

## OBSERVATIONS OF X-RAYS AND THERMAL DUST EMISSION FROM THE SUPERNOVA REMNANT KES 75

TIMOTHY D. MORTON<sup>1</sup>, PATRICK SLANE<sup>2</sup>, KAZIMIERZ J. BORKOWSKI<sup>3</sup>, STEPHEN P. REYNOLDS<sup>3</sup>, DAVID J. HELFAND<sup>4</sup>,  
B. M. GAENSLER<sup>5,2</sup>, AND JOHN P. HUGHES<sup>6</sup>

*To Appear in The Astrophysical Journal*

### ABSTRACT

We present *Spitzer Space Telescope* and *Chandra X-ray Observatory* observations of the composite Galactic supernova remnant Kes 75 (G29.7–0.3). We use the detected flux at 24  $\mu\text{m}$  and hot gas parameters from fitting spectra from new, deep X-ray observations to constrain models of dust emission, obtaining a dust-to-gas mass ratio  $M_{\text{dust}}/M_{\text{gas}} \sim 10^{-3}$ . We find that a two-component thermal model, nominally representing shocked swept-up interstellar or circumstellar material and reverse-shocked ejecta, adequately fits the X-ray spectrum, albeit with somewhat high implied densities for both components. We surmise that this model implies a Wolf-Rayet progenitor for the remnant. We also present infrared flux upper limits for the central pulsar wind nebula.

*Subject headings:* dust, extinction – ISM: individual (SNR G29.7-0.3) – supernova remnants – X-rays: ISM

### 1. INTRODUCTION

The Galactic supernova remnant (SNR) Kes 75, together with its associated pulsar (PSR J1846-0258) and pulsar wind nebula (PWN), is a prototypical example of a composite supernova remnant. Located at a distance of  $d \sim 19d_{19}$  kpc (based on neutral hydrogen absorption measurements – Becker & Helfand 1984) the pulsar luminosity is extremely high – second only to the Crab for Galactic pulsars. PSR J1846-0258 also has an exceptionally strong dipole magnetic field ( $\sim 5 \times 10^{13}$  G), as inferred from the pulsar spin properties (Gotthelf et al. 2000), and the X-ray luminosity from the associated PWN is a remarkably high fraction of the pulsar’s total spindown energy loss (20%, compared to a typical value of  $\sim 0.1\%$ )<sup>7</sup>. The characteristic age of the pulsar is extremely young – only 723 years (Gotthelf et al. 2000) – and recent timing measurements of the braking index,  $n$ , have yielded an estimated upper limit to its true age of only 884 years (assuming  $n$  is constant; Livingstone et al. 2006), placing it among the youngest known rotation-powered pulsars in the Galaxy. The remnant is also quite large ( $\sim 10$  pc in radius), implying an average expansion velocity of  $\sim 10^4$  km/s – typical (or even in excess) of values for undecelerated SNR expansion.

Kes 75 has been studied in considerable detail in both the radio and X-ray bands, but high extinction due to its large distance and location near the Galactic plane prevent its detection at optical wavelengths. In the radio, a synchrotron shell is observed, with a flux density of 10 Jy at 1 GHz, and spectral index  $\alpha = 0.7$  (energy flux  $S_\nu \propto \nu^{-\alpha}$ ), as well as flatter ( $\alpha \sim 0.25$ ) emission from the PWN (Becker & Kundu 1976). Observations with the *ASCA* observatory reveal distinct spec-

tral components from the PWN and the remnant shell (Blanton & Helfand 1996), although the SNR plasma parameters are poorly determined due, in part, to mixing of these two spectral components as a result of the poor angular resolution. Similar morphology to that seen in the radio band has been detected in the X-rays (Helfand et al. 2003 - hereafter H03), with spatial coincidence of the thermal X-ray emission and radio shell (see Figure 1), and an axisymmetric PWN structure with a photon index of  $\Gamma = 1.92$  (photon number flux  $F_\gamma \propto \nu^{-\Gamma}$ ).

While radio and X-ray observations provide information regarding the age, energetics, and ambient conditions for SNRs, infrared observations of remnants are also instructive because they can reveal the presence of heated dust, both shock-heated swept-up dust from the circumstellar or interstellar medium (CSM/ISM), and potentially, dust created by the supernova itself. The Galactic Legacy Infrared Mid-Plane Survey Extraordinaire (GLIMPSE; Benjamin et al. 2003), which uses all four bands of the Infrared Array Camera (IRAC) on the *Spitzer Space Telescope* (*SST*; 3.6, 4.5, 5.8, and 8  $\mu\text{m}$ ), encompassed  $\sim 100$  known radio/X-ray SNRs, about 10-15% of which were detected with confidence (Lee et al. 2005, Reach et al. 2006). Kes 75 was not detected in the GLIMPSE data, nor in earlier infrared SNR surveys (e.g. Arendt 1989, Saken et al. 1992).

As part of a general *SST* survey of LMC SNRs, Borkowski et al. (2006: B06) and Williams et al. (2006a; W06) reported detection of four Type Ia remnants and four core-collapse remnants, respectively, in the 24  $\mu\text{m}$  and 70  $\mu\text{m}$  MIPS (Multi-band Imaging Photometer for *Spitzer*) bands, with stringent upper limits on emission from the IRAC bands. Using these observations in connection with dust emission models, they find evidence of substantial dust destruction in the blast waves of both types of remnant: 30% – 40% of the total dust mass, and as much as 90% of the mass in grains smaller than about 0.04  $\mu\text{m}$ . They find no evidence for emission associated with ejecta. Both studies report pre-shocked dust/gas mass ratios lower by a factor of several than are generally assumed for the LMC.

In order to explore evolutionary scenarios and investigate the dust content in Kes 75, we present X-ray spectral fits for the remnant from new *Chandra* observations, as well as the first infrared detection of this remnant from new *SST* observations. These infrared observations have high enough an-

<sup>1</sup> Harvard College, Cambridge, MA 02138.

<sup>2</sup> Harvard-Smithsonian Center for Astrophysics, 60 Garden Street, Cambridge, MA 02138.

<sup>3</sup> Department of Physics, North Carolina State University, Box 8202, Raleigh, NC 27695-8202.

<sup>4</sup> Columbia Astrophysics Laboratory, Columbia University, 550 West 120th Street, New York, NY 10027.

<sup>5</sup> School of Physics A29, The University of Sydney, NSW 2006, Australia.

<sup>6</sup> Department of Physics and Astronomy, Rutgers University, 136 Frelinghuysen Road, Piscataway, NJ 08854.

<sup>7</sup>  $L_{x,psr}(0.5 - 10 \text{ keV}) = 4.4 \times 10^{35} \text{ ergs s}^{-1}$ ;  $L_{x,neb}(0.5 - 10 \text{ keV}) = 1.7 \times 10^{36} d_{19}^2 \text{ ergs s}^{-1}$  (H03);  $\dot{E} = 8.3 \times 10^{36} \text{ ergs s}^{-1}$  (Livingstone et al. 2006)

gular resolution that, in addition to determining properties of the remnant shell, we are also able to place constraints on infrared emission from the central PWN in order to investigate the need for the spectral break that most PWNe exhibit between the radio and X-ray bands.

## 2. OBSERVATIONS AND DATA REDUCTION

X-ray observations of Kes 75 were carried out in October 2000, for a total of  $\sim 39$  ks, and in June 2006, over four pointings with a total exposure time of  $\sim 156$  ks. Observations were made with the Advanced CCD Imaging Spectrometer (ACIS) instrument on board the *Chandra X-ray Observatory* (CXO), providing a spatial resolution of  $0.5''$  over the range 0.5–10 keV. All data were re-processed using the most recent calibration files, and cleaned for episodes of high background. The total good exposure time for the five pointings was  $\sim 188$  ks. Figure 1 (bottom) shows the X-ray image displayed with a logarithmic intensity scale, showing the both the central PWN and the remnant shell.

Infrared observations were made on September 15, 2005, using both the IRAC and MIPS cameras on the *SST*, and were processed and mosaiced using standard pipelines. Images were obtained at 3.6, 4.5, 5.8, 8, and  $24 \mu\text{m}$ , the shorter wavelength images from the IRAC instrument and the  $24 \mu\text{m}$  image from MIPS. The pixel size is  $1.2''$  for the IRAC bands and  $2.45''$  for MIPS, roughly matched to the (wavelength-dependent) diffraction-limited point spread function of the telescope. For each of the IRAC bands, we obtained a 36-point dither pattern of pointings at the source, with a 30 s integration time per pointing, yielding a total exposure of 1080 s. For the MIPS data, we obtained a total of 4.5 ks using a series of 30 s integrations.

The remnant is not detected in any of the IRAC bands, but the two limbs of the shell apparent in the radio and X-ray images are clearly visible at  $24 \mu\text{m}$ . Figure 1 (middle) shows the  $24 \mu\text{m}$  image, overlaid with X-ray contours to highlight the similarities in morphology. Because Kes 75 lies in the Galactic plane, there is considerable contamination from foreground and background emission. The central PWN is not detected in any of the infrared bands.

To extract X-ray spectra, we used the ‘specextract’ routine in the CIAO software package, grouping to obtain a minimum of 25 counts/bin. We extracted individual spectra for each observation segment using extraction regions corresponding to the southeast (SE) and southwest (SW) limbs and to the PWN, with a background region outside the shell (Figure 1, bottom). We used these same regions to extract infrared fluxes from the *SST* images. X-ray spectral fitting (discussed in greater detail below) was done using the XSPEC software package.

## 3. ANALYSIS

To characterize the X-ray spectrum of the remnant shell, we fit the data to a non-equilibrium ionization (NEI) collisional plasma plane-shock model (an updated version of the XSPEC model ‘vpshock’) with foreground absorption. We fit the spectrum of each limb independently, jointly fitting spectra from each of the observation segments. We find significant excess at the high energy end of the spectrum, consistent with previous fits of X-ray data for Kes 75 (H03). H03 discuss possible origins of this hard tail, such as cosmic-ray acceleration at the shock front or foreground dust-scattering of emission from the PWN, and add a power law component to the model to account for this emission. We find that even with the addition of a power law, the model fits to the spectra are poor

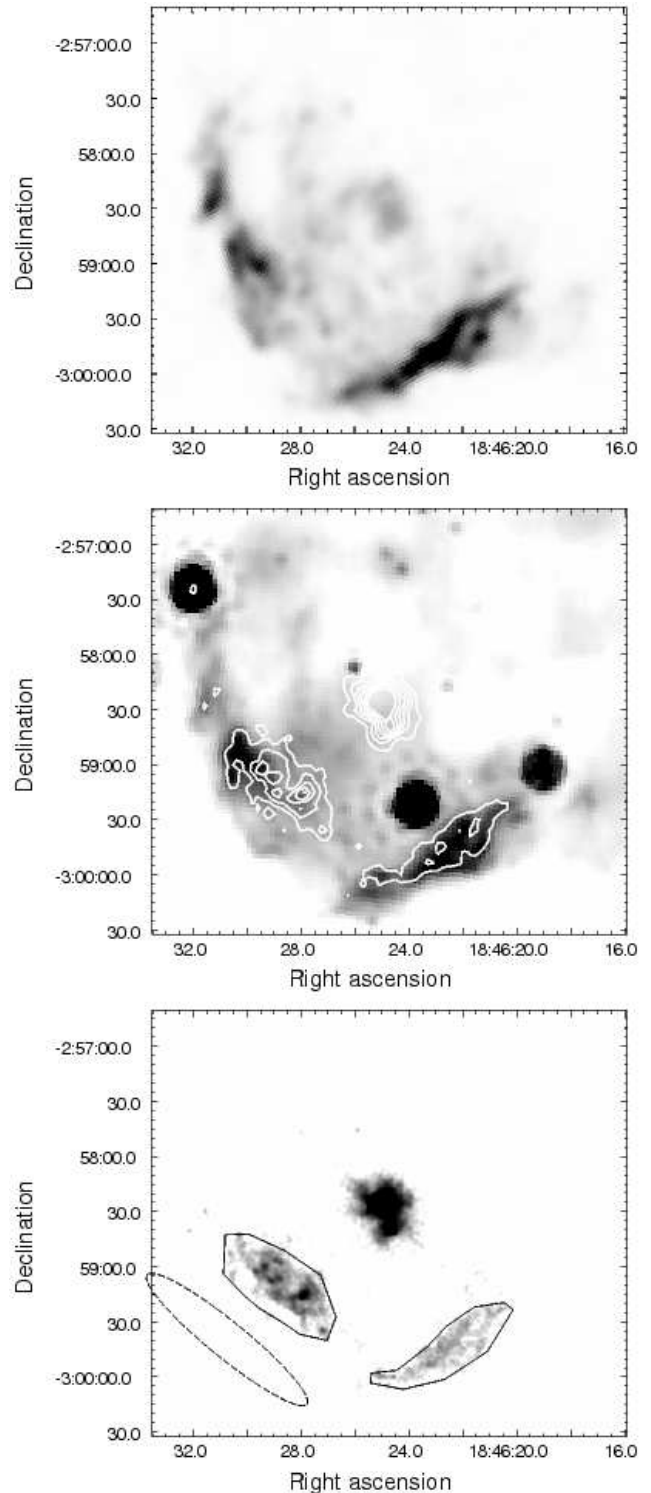


FIG. 1.— Top: VLA image of Kes 75 at 1.4 GHz from the MAGPIS project (Helfand et al. 2006). The greyscale is linear, covering a range of 0 to 0.1 Jy beam<sup>-1</sup>. Middle:  $24 \mu\text{m}$  MIPS image of Kes 75. X-ray contours are overlaid to highlight the similar morphology. The PWN is not detected in the infrared, nor is any part of the shell of Kes 75 detected in any of the IRAC bands. The greyscale is logarithmic, from 100 to 200 MJy sr<sup>-1</sup>. The bright, circular sources in the image, as well as numerous fainter sources, are consistent with point sources along the line of sight to Kes 75. Bottom: *Chandra* X-ray image of Kes 75. Intensity is displayed logarithmically from 10 to 140 cts arcsec<sup>-2</sup>. Extraction regions for the shell and background are shown.

TABLE 1  
INFRARED FLUX DENSITIES

region	3.6 $\mu\text{m}$	4.5 $\mu\text{m}$	5.8 $\mu\text{m}$	8 $\mu\text{m}$	24 $\mu\text{m}$
Thermal shell	<0.04	<0.05	<1.92	<0.72	$18.9 \pm 3.6$
PWN	<0.068	<0.061	<0.044	<0.062	<0.66

NOTE. — All flux densities are extinction-corrected and quoted in Jy. The 3.6, 4.5, 5.8, and 8  $\mu\text{m}$  data are taken with the IRAC instrument, and the 24  $\mu\text{m}$  data with the MIPS camera.

(with a reduced chi-squared  $\chi_r^2 > 1.6$ ), the primary problem being significant residuals around prominent emission lines, and in a broad band near 1 keV.

As an alternative to the power law component, we investigated fits with a second, higher temperature thermal component. As we describe below, this two-component thermal model yields significantly better fits, with the high-temperature component accommodating the hard emission. This component requires enhanced abundances of Si, S, Ar, and Fe, suggesting a scenario in which the low-temperature component corresponds to forward-shocked circumstellar/interstellar material while the high-temperature component originates from reverse-shocked ejecta.

Modeling collisionally heated dust requires the infrared data as input, as well as the hot electron gas density  $n_e$ , electron temperature  $T_e$ , ion temperature  $T_i$ , shock timescale  $\tau = n_e t_{shock}$ , and volume emission measure  $EM = n_e n_H V$ . We are only able to measure directly  $T_e$  from the X-ray spectrum, and we assume  $T_i = T_e$ . This assumption may be incorrect, particularly given the young age of the remnant, but we note that at temperatures of about 1 keV, electron collisions are expected to dominate grain heating (Dwek and Arendt 1992), and so any additional effect from a slightly higher ion temperature would make only a marginal contribution to an increase in emission from the dust. All these parameters, together with standard grain size and composition distribution assumptions (Weingartner & Draine 2001), give a predicted infrared emission spectrum shape, the normalization of which can be adjusted to fit the observed infrared flux. This, in turn, gives a value of the dust-to-gas mass ratio. With this in mind, we note that if ion temperatures are higher than electron temperatures, we will overestimate the amount of dust present, since higher temperatures would require less dust to produce the same emission at a given wavelength. The reader is referred to B06 for a detailed description of the dust modeling.

B06 also used the measured infrared flux values and the 70/24  $\mu\text{m}$  flux ratio to further constrain these models and to make a prediction about dust destruction (since a larger-than-expected 70/24  $\mu\text{m}$  ratio would imply destruction of the smaller grains). However, in the absence of data in the 70  $\mu\text{m}$  band, we had to rely on our 24  $\mu\text{m}$  detection and IRAC band upper limits for our constraints.

In order to extract infrared fluxes, we defined source regions consistent with the emission observed in the Chandra images, excluded any obvious point sources from the infrared data, and then calculated a total background-subtracted flux with the “funtools” package in ds9, using three different background regions for each infrared image. For the 24  $\mu\text{m}$  detection, we averaged the calculated background-subtracted flux for the three different background regions, while for the IRAC images, we used the highest value attained from the three different backgrounds to get conservative flux upper limits. PWN upper limits were obtained in a similar manner. For-

mal errors for the infrared flux extractions were determined from the width of histograms of pixel values in the region, and were determined to be on the order of 10%. The errors we quote, however, are dominated by uncertainties in the background caused by confusion along the line of sight, which we quantify as the largest deviation from the mean of the three background-subtracted results.

To calculate the hot gas densities required to constrain the dust models, we use the volume emission measure ( $n_e n_H V$ ), taken directly from the normalization of the XSPEC ‘vp-shock’ model:

$$K = 10^{-14} \frac{n_e n_H V}{4\pi d^2} \text{ cm}^{-5} \quad (1)$$

where  $n_e$  is the electron density,  $n_H$  is the gas density,  $V$  is the volume of the emitting region, and  $d$  is the distance to the remnant. To calculate the volume of the emitting regions, we take the area of the regions indicated in Figure 1 (bottom) and assume a slab-like volume whose depth along the line of sight is equal to the length of the long axes of the regions. We expect this method to give an upper limit to the volume estimate, so we introduce a filling factor  $0 < f < 1$  to represent the total fraction of the volume that is actually emitting; the filling factors could be considerably smaller than 1 if there is significant clumping in the gas. We then assume that  $n_e/n_H = 1.18$ , which is true for a fully ionized gas with solar abundances, and that  $d = 19$  kpc.

## 4. RESULTS

### 4.1. SNR Infrared flux

We do not detect Kes 75 in any of the four IRAC bands, but we do find a clear detection in the 24- $\mu\text{m}$  MIPS band. This is consistent with the B06 and W06 LMC SNR results, for which detections were only found in the MIPS bands, and with the GLIMPSE SNR results which detected only  $\sim 10\%$  of known Galactic SNRs in the IRAC bands. Infrared flux results are presented in Table 1, where we have corrected the observed flux values using extinction corrections from Indebetouw et al. (2005).

### 4.2. X-ray spectral fitting

As a starting point to spectral fitting of the shell emission from Kes 75, we determined the column density of the foreground gas through fits to the PWN spectrum. We extracted spectra from the five observation segments using a circle centered on the pulsar, with a 7 arcsec radius, but excluding emission from the pulsar itself. An absorbed power law provided an excellent fit to the  $\sim 64000$ -count spectrum ( $\chi_r^2 = 1.01$ ), with  $\Gamma = 1.96 \pm 0.04$  and  $N_H = (4.03 \pm 0.07) \times 10^{22} \text{ cm}^{-2}$ . The  $\sim 40000$ -count spectrum from an annulus extending from a radius of 7 arcsec to 15 arcsec, excluding a small circle around a jet-like feature, gave best-fit values of  $\Gamma = 2.11 \pm 0.05$  and  $N_H = (4.04 \pm 0.10) \times 10^{22} \text{ cm}^{-2}$  ( $\chi_r^2 = 0.99$ ). Details of the spectrum and structure of the PWN are the subject of a forthcoming paper. Based on the above fits, we adopt a value of  $N_H = 4 \times 10^{22} \text{ cm}^{-2}$  for the shell of Kes 75. We note that this value is in excellent agreement with that derived by H03 through fits to the PWN.

The shape of the high energy continuum (above 3 keV) for the SNR shell is consistent with a bremsstrahlung model with  $kT \sim 1.8$  keV. With  $N_H$  fixed as described above, extrapolating back to lower energies yields a large deficit relative to the observed flux in the 1–2 keV band; an additional soft

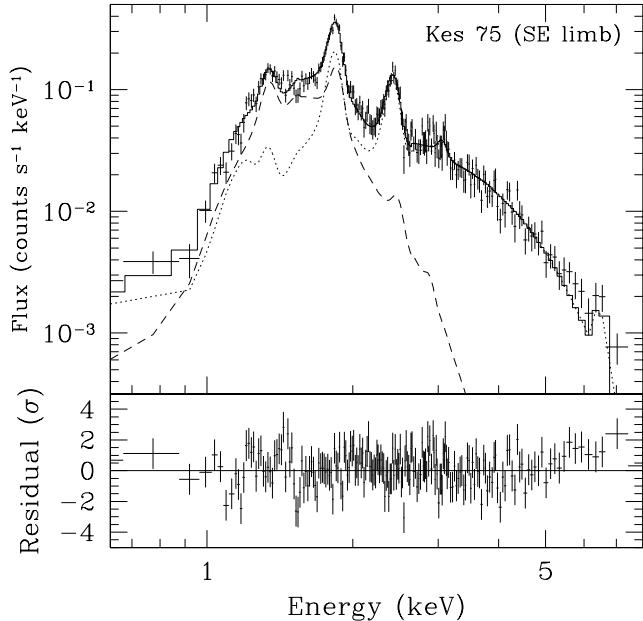


FIG. 2.— The spectrum of the Kes 75 thermal shell (SE limb, taken from a 54 ks segment of *Chandra* data), with a two-component thermal model. Dashed (dotted) curves show the low (high) temperature thermal model components.

thermal component is required. We thus investigated a model with two vps shock model components, one with a temperature near that from the bremsstrahlung model, and one set lower to accommodate the soft emission. We allowed the temperature, ionization timescale, and normalization to vary for each of the thermal components, and find that significant residuals remain around the lines of Si, S, and Ar, as well as in a broad band near  $\sim 1$  keV, where Fe-L emission dominates. When the abundances of these elements are allowed to vary (independently) in the high temperature component, we find a much-improved fit with large enhancements above solar values. In Figure 2 we plot the spectrum of the SE limb from one of the observation segments. Also shown is the best-fit model, as well as each individual emission component. Fitting results are summarized in Table 2, where the errors on the fit parameters represent 90% confidence intervals.<sup>8</sup>

While the X-ray spectrum from an SNR is, in reality, comprised of emission from a distribution of temperatures, compositions, and ionization states, we broadly associate the low-temperature component found here with the forward-shocked CSM/ISM, and the high-temperature, metal-enriched component with the reverse-shocked ejecta. The ionization timescales for the CSM/ISM component are poorly constrained on the high end, and we are only able to reliably obtain lower limits. The fits are remarkably similar for the two limbs, particularly given the considerable difference in X-ray/IR flux ratios observed in Figure 1. The best-fit model for the SE limb, which has a higher X-ray flux than the SW limb, yields a slightly higher swept-up CSM/ISM temperature and a slightly lower ejecta temperature, but these variations are not of high statistical significance. We do not find any evidence

<sup>8</sup> We note that H03 find similar  $\chi_r^2$  values for an ad hoc model of bremsstrahlung emission accompanied by gaussian lines at discrete energies, but reject this model as non-physical based on the lack of connection between derived temperature and the centroids and relative strengths of the lines.

TABLE 2  
SPECTRAL FITS TO THE KES 75 THERMAL SHELL

Parameter	SE Rim	SW Rim
$N_H$ ( $\times 10^{22}$ cm $^{-2}$ )	4.0 (fixed)	4.0 (fixed)
$kT_1$ (keV)	$0.25 \pm 0.01$	$0.22 \pm_{0.01}^{0.02}$
Abundances	solar	solar
$\tau_1$ (s cm $^{-3}$ )	$> 1.5 \times 10^{12}$	$> 1.5 \times 10^{12}$
$F_1^a$ ( $\times 10^{-10}$ ergs cm $^{-2}$ s $^{-1}$ )	4.6	2.2
$kT_2$ (keV)	$1.38 \pm 0.02$	$1.50 \pm_{0.07}^{0.98}$
[Si] <sup>b</sup>	$3.7 \pm 0.2$	$3.6 \pm 0.5$
[S]	$13.5 \pm 0.7$	$10.2 \pm 1.3$
[Ar]	$10.5 \pm 2.3$	$6.9 \pm_{3.2}^{3.4}$
[Fe]	$14.5 \pm 1.8$	$14.2 \pm_{4.3}^{5.2}$
$\tau_2$ (s cm $^{-3}$ )	$(7.0 \pm 0.3) \times 10^9$	$(6.1 \pm 0.4) \times 10^9$
$F_2$ ( $\times 10^{-10}$ ergs cm $^{-2}$ s $^{-1}$ )	2.2	1.0
$\chi_r^2$ (dof)	1.34 (840)	1.31 (522)

<sup>a</sup> X-ray fluxes are unabsorbed in the 0.5 - 10 keV band.

<sup>b</sup> Abundances are relative to solar values.

for spectral variations within the limb regions, although the reduction in the number of counts in each spectrum results in a corresponding increase in the fit uncertainties, limiting our ability to discern small spatial variations that might be expected from the two emission components.

### 4.3. Densities and Shock Ages

As described above, we can estimate the densities of the emission components from the normalization provided by the X-ray model fits along with an estimate of the emitting volume (Eq. 1). Using values from Table 2, we find filling-factor-dependent post-shock electron densities for both the swept-up CSM/ISM component and ejecta component from each limb. The values we get are fairly high, especially for the CSM/ISM component ( $58f_1^{-1/2}d_{19}^{-1/2}$  cm $^{-3}$  and  $36f_1^{-1/2}d_{19}^{-1/2}$  cm $^{-3}$  for the SE and SW limbs, respectively). In addition, even with these high densities, the forward shock ages implied from the measured ionization timescales ( $>2400$  yrs) are significantly higher than current best estimates of the pulsar age from spindown measurements ( $<900$  yrs). For the reverse shock, we obtain more modest densities of  $\sim 9.6f_2^{-1/2}$  cm $^{-3}$  ( $\sim 2.2f_2^{-1/2}$  cm $^{-3}$ ) for the SE (SW) region, and an age of around 75 years, which, though young, is not completely implausible for recently shocked ejecta. We scale quantities with different filling factors  $f_1$  and  $f_2$  to indicate the possibility that the two emission components may occupy different fractions of the total volume (but we treat these as being the same in the SE and SW limbs). We note that the density estimate for the ejecta component (which comprises the bulk of the observed flux, but a considerable minority of the unabsorbed flux) is similar to that obtained for a single thermal component by H03. It is a factor of  $\sim 5$  higher than that obtained by Blanton & Helfand (1996), but this is primarily because they assumed that the emission completely filled a shell around the PWN (since ASCA was unable to resolve the emission and show that the thermal component was primarily from the much smaller SE and SW limbs).

### 4.4. Dust models

The measured 24  $\mu$ m fluxes of 2.4 Jy and 2.8 Jy in the SE and SW limbs, respectively, can be used to estimate dust

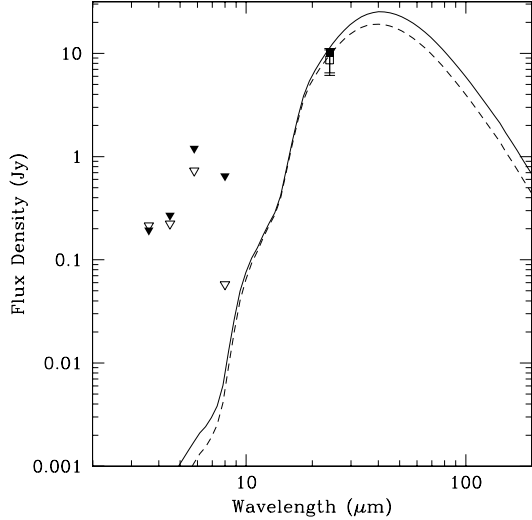


FIG. 3.— Dereddened IR emission from the shell of Kes 75, along with the dust-emission model described in the text. Inverted triangles indicate upper limits. Filled symbols and the solid curve correspond to the SW shell while open symbols and the dashed curve correspond to the SE shell. The model is derived from the electron temperature and density implied by the X-ray measurements, with the  $24\mu\text{m}$  measurements setting the normalization for the hydrogen density.

masses present in the shocked ambient medium. Here we treat the IR emission as arising exclusively from dust. This is consistent with the X-ray results that indicate a swept-up CSM/ISM mass that is a factor of  $\sim 6$  larger than the X-ray-emitting ejecta mass. The high ( $4 \times 10^{22} \text{ cm}^{-2}$ ) column density  $N_H$  toward Kes 75 implies a very high ( $A_V \sim 22^m$ ) optical extinction, and substantial extinction ( $A_{24\mu\text{m}} = 1.4$ ) even in the MIPS  $24 \mu\text{m}$  band (we used an infrared extinction curve from Chiar & Tielens 2006 valid for the local diffuse ISM). The dereddened  $24 \mu\text{m}$  fluxes are 8.7 Jy and 10.2 Jy in the SE and SW limbs, respectively. Because the shape of the IR spectrum is not known, we must rely on modeling in making dust mass estimates. As described in Section 3 (and, in more detail, in B06), the spectral shape is determined by the grain temperatures, which depend primarily on the temperatures and densities of the X-ray emitting plasma. The electron temperatures are 0.25 keV and 0.22 keV in the SE and SW limbs (Table 2). A lower limit to the electron densities,  $50 \text{ cm}^{-3}$ , is obtained from limits on  $\tau$  listed in Table 2 and the SNR age  $t_{\text{SNR}}$  of less than 884 yr (Livingstone et al. 2006). Electron densities derived from emission measures depend on the unknown filling fraction  $f$ ; by setting  $f = 1$  and assuming a distance of 19 kpc, we obtain comparable density lower limits of  $58 \text{ cm}^{-3}$  and  $36 \text{ cm}^{-3}$  in SE and SW limbs, respectively. The spectral energy distribution predicted from these inputs, and constrained by the observed  $24\mu\text{m}$  flux, is plotted in Figure 3. Triangles indicate upper limits from the IRAC data, and squares represent the measured flux from the MIPS data.

The estimated dust masses are  $0.03 M_\odot$  and  $0.05 M_\odot$  in SE and SW, for plane shocks with age of 884 yr, and temperatures and density upper limits just quoted. These dust masses should be considered as upper limits to the actual dust masses in the limbs, as less dust is required to produce the observed fluxes at higher plasma densities (which would be implied for filling factors smaller than the assumed value). About 40% of the preshock dust mass was destroyed by sputtering in these shock models; dust destruction rates are higher

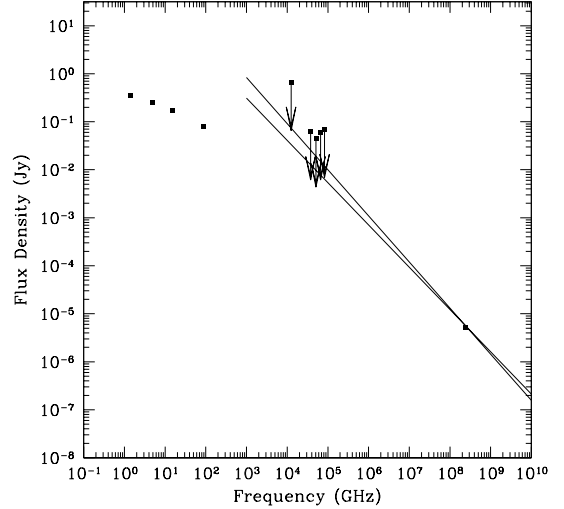


FIG. 4.— The PWN spectrum. Note the spectral break necessary between the radio points (from Salter et al. 1989; Bock and Gaensler 2005) and the X-ray regime (Helfand et al. 2003). Our infrared upper limits are consistent with both X-ray and radio data (marginally so with X-ray at the  $8 \mu\text{m}$  point) suggesting a spectral break in or near the infrared.

at higher densities. In addition, IR line emission from [Fe II] or [O IV], which been observed in N49 (Williams et al. 2006b) and has been suggested as a contributor to the emission from 1E 0102.2-7219 (Stanimirović et al. 2005), may contribute a small fraction of the flux from the ejecta component in Kes 75. If present, this will further reduce our dust mass estimates. We note that we have assumed a grain size distribution and composition that is typical of the Milky Way ISM. With a detection at only one wavelength in the IR, the data are not sufficient to probe potential variations from these values.

#### 4.5. PWN spectrum

We do not detect the central PWN in any of the *SST* bands we observed, but we list upper limits to the flux in Table 1, and we plot these (in Figure 4) against current radio and X-ray data from Salter et al. (1989), Bock and Gaensler (2005), and H03. We find that the IRAC upper limits do not introduce stringent constraints on the spectral break frequency. While a change in spectral index is required between the radio and X-ray bands, with extrapolation of the radio and X-ray spectra indicating a break somewhere near the IR band, the *SST* data do not constrain where this break occurs.

## 5. DISCUSSION

### 5.1. The remnant's shell

Using our density estimates from both limbs to calculate the total gas masses, we find  $\sim 94 f_1^{1/2} d_{19}^{5/2} M_\odot$  for the cool forward-shock component and  $\sim 15 f_2^{1/2} d_{19}^{5/2} M_\odot$  for the ejecta component, where we have added the contributions for the two shells. The value for the CSM/ISM component is particularly high, especially given the large expansion velocity implied by the inferred size and age, although clumping of the gas (i.e., a smaller filling factor) would yield smaller values. We also note that these estimates correspond only to the observed shell segments, which occupy roughly 20-30% of the circumference of the remnant.

While the adopted two-component thermal model provides

an adequate fit to the X-ray spectrum of Kes 75, it is clearly only an approximation for the forward and reverse shock emission components. We are unable to constrain more complex distributions of the temperature, ionization state, and abundances, particularly given the very high absorption, but we believe that the distinct components identified in the spectral fits provide adequate evidence to identify the presence of shocked CSM/ISM material in the presence of enriched ejecta. We note, however, that the high Fe abundance inferred for the ejecta component is problematic in that it implies much higher amounts of Fe than expected for a very massive stellar progenitor. While the uncertainties listed in Table 2 correspond to formal  $\chi^2$ -fitting errors, the enhanced Fe abundance is preferred by the fits solely to reduce residuals in the broad Fe-L region near  $\sim 1$  keV, where the high absorption makes it particularly difficult to rule out a more complex temperature distribution for the forward shock component that could potentially reduce these residuals.

### 5.2. The remnant's dust content

The dust/gas mass ratios we find are  $5 \times 10^{-4}$  and  $1.4 \times 10^{-3}$  for the SE and SW limbs, respectively. These are considerably smaller than the value of  $\sim 0.7\%$  normally assumed for the Galaxy. The nominal Galactic value is calculated by measuring the extinction from nearby bright stars; using SNRs to probe dust provides a different sample of the ISM dust content in the Galaxy, potentially affected by local grain destruction by the SNR shock (which may represent as much as 40% of the dust mass in the preshock material, as described in Section 4.4). We note that the dust mass estimates are based on the assumption that all of the IR emission results from dust. Any contribution from line emission would reduce the dust/gas mass ratio even further. We also note, though, that the gas mass values are derived from the low-temperature component of a heavily absorbed X-ray spectrum.

Our low dust/gas ratio is consistent with the results reported by B06 and W06 in the LMC, who found discrepancies of factors of  $\sim 5$  between their deduced dust/gas ratios and the (lower than Galactic) values commonly assumed for the LMC. W06 speculate that if grains are porous, smaller dust masses could provide the observed extinctions, while larger masses would be required to produce the observed IR emission because of more efficient dust destruction, bringing the two types of estimates closer together.

In order to place better constraints on the dust component, additional infrared observations are required. Infrared spectra would more tightly constrain the dust models and allow us to state more confidently the dust composition of the remnant. A spectrum would also reveal how much, if any, of the  $24 \mu\text{m}$  flux might be from emission lines (such as [Fe II] or [O IV]) rather than emission from heated dust.

### 5.3. The remnant's progenitor

Chevalier (2005) discusses the origins and evolution of massive star core-collapse supernovae, to which class Kes 75 belongs, and notes in particular that Kes 75 has characteristics suggestive of an origin from a Type Ib or Type Ic event. SN Ib/c are born from Wolf-Rayet (WR) stars, which are characterized by high mass-loss rates, and especially high-velocity stellar winds. These WR winds are 100-200 times faster than winds from earlier mass-loss stages, and so they sweep up the circumstellar medium and slow-velocity wind material, and clear out a bubble around the star, bounded by a dense and

clumpy shell extending up to  $\geq 10$  pc over a WR lifetime of  $\sim 2 \times 10^5$  yr. Thus, when the star finally collapses and produces a SN Ib/c, the ejecta travel initially through very low-density gas, and then eventually begin to interact with this dense WR shell.

Assuming a WR picture for a progenitor for Kes 75 answers several questions, most prominently the large size of the remnant: if ejecta are able to expand uninhibited through a low-density medium (cleared out by the WR wind), then they will not sweep up mass quickly, and thus will not slow down significantly. This indication, and the young shock age of the reverse-shocked ejecta (implying recent shocking of the WR shell), both point to this progenitor model. This bubble model might also help explain the high density and clumpiness that we seem to be observing, and mixing of ejecta and swept-up material across the contact discontinuity due to the interaction with a dense shell may explain the lack of any obvious spatial separation of these components. Finally, dust depletion by the WR wind could also contribute to the very low inferred dust-to-gas ratio in Kes 75.

The X-ray luminosity for Kes 75, based on the flux values from Table 2, is extremely high ( $L_x = 4.3 \times 10^{37} d_{19}^2 \text{ ergs s}^{-1}$ ). Nearly 70% of this luminosity can be attributed to the low-temperature emission component, and this raises the concern that most of this inferred emission is actually hidden by the high column density. As noted above, a more complex temperature distribution for this component could yield a significantly different unabsorbed result. However, the luminosity for the higher temperature component is exceptionally large as well, as is that for the pulsar and the PWN. This could point to an error in the distance estimate of 19 kpc. However, a rather large error would be required. To reduce  $L_{x,pwn}/\dot{E}$  to a value of 1% – similar to that for the Crab, but still a factor of 10 larger than the (very broad) average for PWNe – would require a distance reduction by a factor of 4.5. This would reduce the remnant radius and inferred free-expansion speed by the same factor, and reduce the mass estimates by a factor of nearly 40. However, this distance would double the already-high inferred density of the postshock gas, and the observed column density would be anomalously high. If, instead, the interpretation of a distant WR progenitor is correct (and we infer this based on several lines of reasoning), then Kes 75 is the remnant of a relatively rare event, and perhaps the fact that its properties stand out from the rest of the population is not unexpected.

### 5.4. The remnant's PWN

Extrapolation of the radio and X-ray spectra for the PWN in Kes 75 indicate a spectral break near the IR band. The upper limits we derive for the infrared emission are consistent with such a break, but do not provide additional constraints because the values are above the extrapolated break at  $\nu_b \approx 5 \times 10^{14}$  Hz. If interpreted as a synchrotron break, this would indicate a magnetic field  $B \sim 100 \mu\text{G}$  given the age of the pulsar. This is somewhat large value for a PWN, and corresponds to a magnetic energy within the nebula that comprises nearly the entire spin-down energy deposited by the pulsar over its estimated age. The required change in spectral index for such a break is  $\Delta\alpha \approx 0.7$ , which is larger than the change of 0.5 expected purely from synchrotron losses. However, a wide variety of effects can lead to spectral curvature or complex breaks, including structure in the input particle spectrum, nonuniform magnetic fields, and time dependence in the

pulsar input power. Considerably deeper IRAC observations could constrain the spectral behavior between the radio and X-ray bands. Similarly, observations in the submillimeter and TeV bands could potentially probe the mid-frequency behavior of the spectrum as well as the high energy cut-off.

## 6. CONCLUSIONS

Using updated versions of fitting codes and new *Chandra* observations, we model the X-ray spectrum of Kes 75 using a two-component thermal model in which we broadly associate a cool, solar-abundance component with forward-shocked CSM/ISM, and a hot, metal-rich component with reverse-shocked ejecta. The implied gas masses are somewhat high, particularly for the cool component, suggesting that the forward shock has encountered dense ambient material. The fits give ionization timescales for the cool component of  $\tau > 10^{12}$  s cm<sup>-3</sup>, implying an age of > 2400 years (older than the measured spindown age), and of  $\tau < 10^{10}$  s cm<sup>-2</sup> for the hotter, enriched component, implying very recently shocked material ( $\sim 75$  years). This, combined with the large size and high average expansion velocity for the SNR, suggests a Wolf-Rayet progenitor that cleared out a  $\sim 10$  pc bubble before exploding in a type Ib/c supernova.

We also report the detection of Kes 75 at 24  $\mu$ m; the morphology of the infrared emission is spatially coincident with

the observed X-ray shell emission. We use this detection and the parameters derived from the X-ray fits to model the dust emission of this remnant, finding a dust/gas mass ratio of about  $10^{-3}$  or less, considerably lower than the value of  $\sim 0.7\%$  for the Galaxy derived from optical and ultraviolet extinction measurements. Additional infrared observations of Kes 75 at different wavelengths would further constrain this ratio. We do not detect the remnant at shorter wavelengths, indicating the destruction of small grains by the shock. We suggest that the use of high-resolution infrared imaging and X-ray spectroscopy of SNRs to constrain dust models might provide a new sample of Galactic ISM dust measurements, distinct from extinction measurements.

We do not detect the pulsar wind nebula in Kes 75 in any of our infrared observations, primarily due to the high Galactic background. The upper limits we derive are consistent with unbroken extrapolations of the both the radio and X-ray spectra of the nebula, suggesting a spectral break either in the infrared or between the radio and infrared.

The work presented here was supported in part by *Spitzer* Grants JPL CIT 1264892 (DJH), JPL RSA 1264893 (SPR), and JPL 1265776 (POS), as well as Chandra Grant GO6-7053X (POS) and NASA Contract NAS8-39073 (POS).

## REFERENCES

- Arendt, R. G. 1989, *ApJS*, 70, 181  
 Benjamin, R. A. et al. 2003, *PASP*, 115, 953  
 Becker, R. H., & Helfand, D. J. 1984, *ApJ*, 283, 154  
 Becker, R. H., & Kundu, M. R. 1976, *ApJ*, 204, 427  
 Blanton, E. L. & Helfand, D. J. 1996, *ApJ*, 470, 961  
 Bock, D. C.-J., & Gaensler, B. M. 2005, *ApJ*, 626, 343  
 Borkowski, K. J., et al. 2006, *ApJ*, 642, L141 (B06)  
 Chevalier, R. A. 2005, *ApJ*, 619, 839  
 Chiar, J. E., & Tielens, A. G. G. M. 2006, *ApJ*, 637, 774.  
 Dwek, E., & Arendt, R. G. 1992, *ARA&A*, 30, 11  
 Gotthelf, E. V., Vasisht, G., Boylan-Kolchin, M., & Torii, K. 2000, *ApJ*, 542, L37  
 Helfand, D. J., Collins, B. F., & Gotthelf, E. V. 2003, *ApJ*, 582, 783 (H03)  
 Helfand, D. J., Becker, R. H., White, R. L., Fallon, A., and Tuttle, S. 2006, *AJ*, 131, 2525  
 Indebetouw, R. et al. 2005, *ApJ*, 619, 931  
 Lee, H.-G. 2005, *Journal of Korean Astronomical Society*, 38, 385  
 Livingstone, M. A., Kaspi, V. M., Gotthelf, E. V., & Kuiper, L. 2006, *ApJ*, 647, 1286  
 Reach, W. T., et al. 2006, *AJ*, 131, 1479  
 Saken, J. M., Fesen, R. A., & Shull, J. M. 1992, *ApJS*, 81, 715  
 Salter, C. J., Reynolds, S. P., Hogg, D. E., Payne, J. M., & Rhodes, P. J. 1989, *ApJ*, 338, 171  
 Stanimirović, S. et al. 2005, *ApJ*, 632, L103  
 Weingartner, J. C., & Draine, B. T. 2001, *ApJS*, 134, 263  
 Williams, B. J. et al. 2006, *ApJ*, 652, L33 (W06)  
 Williams, R. M. et al. 2006, *AJ*, 132, 1877